Nano Research 2015, 8(11): 3612–3620
DOI 10.1007/s12274-015-0861-4
Research Article
ISSN 1998-0124
CN 11-5974/O4

One-pot synthesis of Bi_2Se_3 nanostructures with rationally tunable morphologies

Xianli Liu[§], Jinwei Xu[§], Zhicheng Fang[§], Lin Lin, Yu Qian, Youcheng Wang, Chunmiao Ye, Chao Ma (✉), and Jie Zeng (✉)

Hefei National Laboratory for Physical Sciences at the Microscale, Key Laboratory of Strongly-Coupled Quantum Matter Physics of Chinese Academy of Sciences, Center of Advanced Nanocatalysis (CAN-USTC) & Department of Chemical Physics, University of Science and Technology of China, Hefei 230026, China
[§] *These authors contributed equally to this work.*

Received: 6 June 2015
Revised: 3 July 2015
Accepted: 12 July 2015

KEYWORDS
shape control,
Bi_2Se_3 nanostructures,
supersaturation,
mechanism study

ABSTRACT

Shape control has proven to be a powerful and versatile means of tailoring the properties of Bi_2Se_3 nanostructures for a wide variety of applications. Here, three different Bi_2Se_3 nanostructures, i.e., spiral-type nanoplates, smooth nanoplates, and dendritic nanostructures, were prepared by manipulating the supersaturation level in the synthetic system. This mechanism study indicated that, at low supersaturation, defects in the crystal growth could cause a step edge upon which Bi_2Se_3 particles were added continuously, leading to the formation of spiral-type nanoplates. At intermediate supersaturation, the aggregation of amorphous Bi_2Se_3 particles and subsequent recrystallization resulted in the formation of smooth nanoplates. Furthermore, at high supersaturation, polycrystalline Bi_2Se_3 cores formed initially, on which anisotropic growth of Bi_2Se_3 occurred. This work not only advances our understanding of the growth mechanism but also offers a new approach to control the morphology of Bi_2Se_3 nanostructures.

1 Introduction

Over the past decades, Bi_2Se_3 has attracted considerable attention owing to its unique structure and promising applications [1–7]. In Bi_2Se_3, five covalently bonded atomic sheets (Se-Bi-Se-Bi-Se) along the *c*-axis compose one quintuple layer (QL, ~1 nm), and these QLs are linked together by van der Waals interactions [8]. As a topological insulator with an insulating bulk phase and an exotic metal surface, Bi_2Se_3 has a remarkable band gap up to 0.3 eV and a single Dirac cone at the Γ points [9, 10]. The unique surface structure leads to the attractive electronic and optical properties of Bi_2Se_3 [11, 12] and thus opens up many important applications including photodetection [13], ultrafast lasers [14], cancer treatment [15], and thermoelectric materials [16–18]. Since these applications are highly sensitive to the size, shape, and structure of

Address correspondence to Chao Ma, cma@ustc.edu.cn; Jie Zeng, zengj@ustc.edu.cn

nanomaterials [19–24], morphological modulation can be introduced as an effective tool to tailor the properties and optimize the performance towards a specific application for Bi_2Se_3 nanostructures.

For these reasons, much effort has been devoted to the preparation of Bi_2Se_3 nanostructures with well-defined morphologies. To date, diverse chemical methods have been adopted to prepare Bi_2Se_3 nanostructures, such as solvothermal synthesis of Bi_2Se_3 nanoplates and nanoflowers [25, 26], photochemical synthesis of Bi_2Se_3 nanospheres and nanorods [27], and polyol synthesis of Bi_2Se_3 nanosheets and architectural nanostructures [28–31]. Recently, our group achieved screw-dislocation-driven bidirectional growth of spiral-type Bi_2Se_3 nanoplates with a bipyramid-like shape [32]. Despite the success of preparing Bi_2Se_3 nanostructures with a fixed shape, a universal system that is of highly amenability to preparing Bi_2Se_3 nanostructures with rationally tunable morphologies has not yet been lucubrated. In addition, a fundamentally significant process during the synthesis, i.e., the growth mechanism, has not been elucidated.

Herein, we demonstrate a polyol synthesis to obtain a set of well-defined Bi_2Se_3 nanostructures. Through fine control of the supersaturation level in the synthetic system, three different types of Bi_2Se_3 nanostructures, i.e., spiral-type nanoplates, smooth nanoplates, and dendritic nanostructures, were successfully prepared. The mechanism study indicated that, at low supersaturation, defects in the crystal growth could cause a step edge, upon which Bi_2Se_3 particles were added continuously, leading to the formation of spiral-type nanoplates. At intermediate supersaturation, the aggregation of amorphous Bi_2Se_3 particles and subsequent recrystallization resulted in the formation of smooth nanoplates. Furthermore, at high supersaturation, polycrystalline Bi_2Se_3 cores were formed initially, on which anisotropic growth of Bi_2Se_3 occurred subsequently. As a result, dendritic nanostructures were obtained in the final products. We believe that the method in this work can be utilized as a guideline to obtain other nanomaterials with rationally tunable morphologies and optimized performance for a given application.

2 Experimental

2.1 Chemicals and materials

Sodium selenite (Na_2SeO_3, 99%), bismuth nitrate pentahydrate ($Bi(NO_3)_3{\cdot}5H_2O$, 99%), L-ascorbic acid (AA), poly(vinylpyrrolidone) (PVP, $M_W \approx 40{,}000$), ethylene glycol (EG, 99%), sodium hydroxide (NaOH), and hydrochloric acid (HCl, 38% in H_2O) were purchased from Sinopharm Chemical Reagent Co. Ltd., Shanghai, China. All chemicals were used as received without further purification. Deionized water with a resistivity of 18.2 MΩ·cm was used for the preparation of NaOH aqueous solution.

2.2 Synthesis of three Bi_2Se_3 nanostructures with different morphologies

Stoichiometric amounts of $Bi(NO_3)_3{\cdot}5H_2O$ (9 mg) and Na_2SeO_3 (4.8 mg) were dissolved separately in 0.45 mL of EG and then injected rapidly into another EG solution (14.1 mL) containing PVP (143 mg), AA (87 mg), and HCl (11.8 M)/NaOH aqueous solution (1 M) at 175 °C under a N_2 atmosphere. Specifically, when adding 100 μL of HCl, 20 μL of HCl, or 20 μL of aqueous NaOH into the mixture, spiral-type nanoplates, smooth nanoplates, or dendritic nanostructures were obtained, respectively. After the reaction finished, the products were precipitated at a rotation speed of 8,000 rpm for 5 min and washed three times by ethanol.

2.3 Instrumentation

Transmission electron microscopy (TEM) images were taken using a Hitachi H-7650 microscope at an acceleration voltage of 100 kV. High-resolution TEM (HRTEM), high-angle annular dark-field scanning TEM (HAADF-STEM), and X-ray energy dispersive spectrometry (EDS) analysis were performed on a JEOL ARM-200F field-emission TEM operating at 200 kV. Atomic force microscopy (AFM) study was performed with a Veeco DI Nano-scope MultiMode V system. X-ray diffraction (XRD) characterization was performed using a Philips X'Pert Pro X-ray diffractometer with a monochromatized Cu Kα radiation source at a wavelength of 0.1542 nm. The extinction

spectra were attained using a U-4100 UV-visible (UV-vis) spectrophotometer (Hitachi, Japan).

3 Results and discussion

3.1 Structural and compositional analysis of Bi_2Se_3 nanostructures with controllable morphologies

In a typical synthesis, $Bi(NO_3)_3{\cdot}5H_2O$ (9 mg) and Na_2SeO_3 (4.8 mg) were dissolved separately in 0.45 mL of EG and then rapidly injected into another EG solution (14.1 mL) containing PVP (143 mg), AA (87 mg), and HCl (11.8 M) held at 175 °C under N_2. As the reaction proceeded, the solution changed color to dark grey, indicating the formation of Bi_2Se_3 nanocrystals. A typical TEM image shows that the Bi_2Se_3 nanocrystals obtained using 100 μL of HCl were hexagonal and plate-like, with a typical lateral size of 1–2 μm (Fig. 1(a)). An individual nanoplate was further characterized by high-magnification TEM analysis (Fig. 1(b)), through which two sets of densely distributed centrosymmetric helical fringes on the surface could be clearly seen. Figure 1(c) presents HAADF-STEM image of a typical spiral-type nanoplate and corresponding elemental mapping by means of EDS. Both Bi (green) and Se (red) were distributed uniformly (Figs. 1(c) and 1(d)). A radical drop in the EDS line-scanning profile indicated a hollow core near the center area of the spiral-type nanoplate (Fig. 1(d)), which was in agreement with our previous work [32]. To better visualize the structure of spiral-type nanoplates, AFM analyses are presented in Fig. 2. The AFM amplitude image in Fig. 2(b) clearly shows a hexagonal nanoplate with helical fringes on the surface. The height profile (Fig. 2(c)) along the black line in Fig. 2(a) indicates that the thickness increased gradually from the edge to the center, which was also confirmed by three-dimensional AFM images (Figs. 2(d) and 2(e)). Bi_2Se_3 nanostructures with different morphologies were obtained by adjusting the pH value of the solution. Smooth nanoplates took the place of spiral-type nanoplates when 100 μL of HCl was switched to 20 μL of HCl with the other conditions unchanged. As shown in Fig. 1(e), the resultant Bi_2Se_3 nanocrystals were hexagonal as well, with an average lateral size of ~3.5 μm. A high-magnification TEM

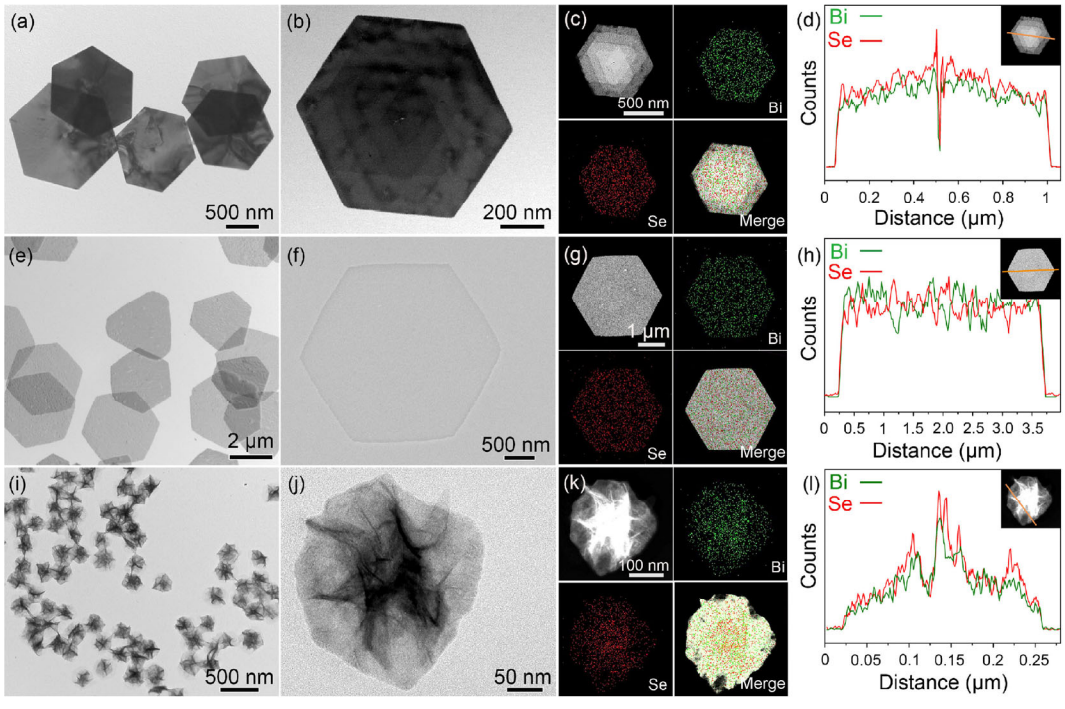

Figure 1 (a), (e), and (i) Low-magnification TEM images of spiral-type Bi_2Se_3 nanoplates, smooth Bi_2Se_3 nanoplates, and dendritic Bi_2Se_3 nanostructures, respectively. (b), (f), and (j) High-magnification TEM images from an individual nanostructure. (c), (g), and (k) HAADF-STEM images and corresponding elemental maps showing the distribution of Bi (green) and Se (red). (d), (h), and (l) Line-scanning EDS profiles for different elements.

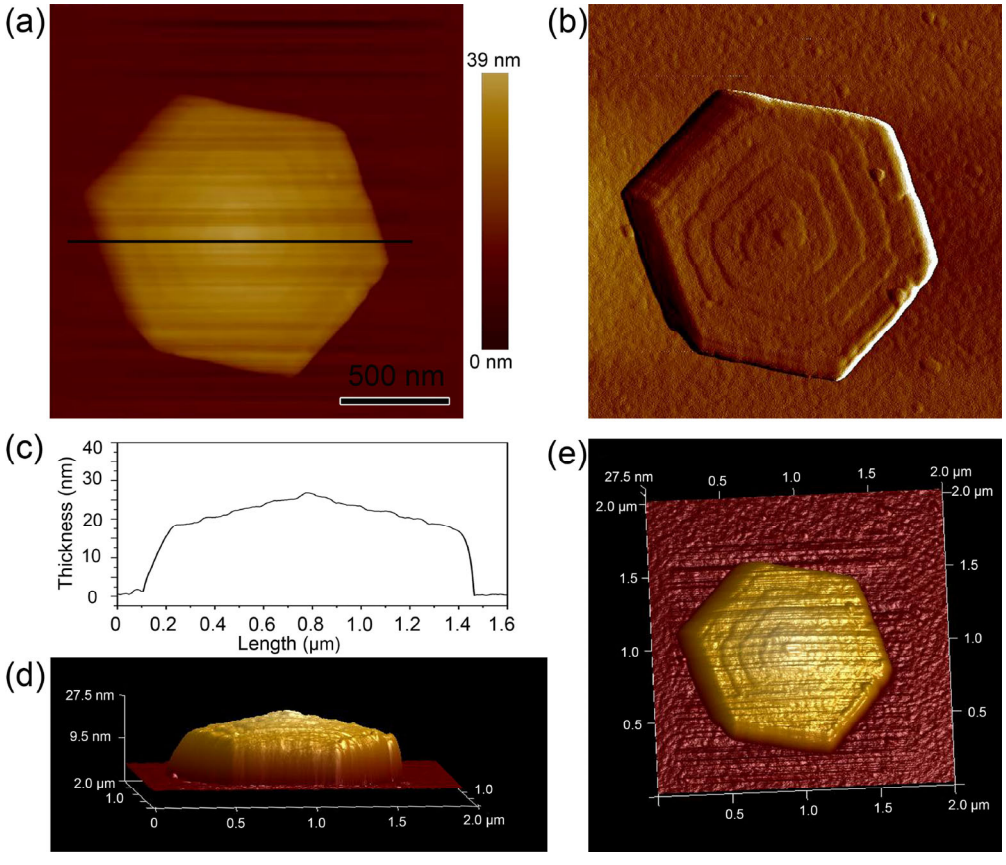

Figure 2 (a) AFM image of an individual spiral-type nanoplate. (b) AFM amplitude image of the nanoplate in (a). (c) AFM height profile along the black line in (a). (d) and (e) Three-dimensional AFM images from the side and top views, respectively.

image indicated that the nanoplate was smooth on the surface, containing no helical fringes, unlike the spiral-type one. Homogeneous distributions of Bi and Se in the smooth nanoplate were revealed by EDS mapping and line-scanning analysis (Figs. 1(g) and 1(h)). No drastic drops were found in the EDS line-scanning profile, supporting the formation of smooth nanoplates with relatively uniform thickness. Dendritic nanostructures were obtained when adding 20 μL of NaOH solution (1 M) instead of HCl with the other conditions unchanged (Fig. 1(i)). A high-magnification TEM image indicated that the dendritic nanostructure was composed of several irregular branches protruding from the center with thin surrounding peripheries (Fig. 1(j)). Similar to the spiral-type and smooth nanoplates mentioned above, the dendritic nanostructure had uniform distributions of Bi and Se as well (Figs. 1(k) and 1(l)). Sharply fluctuating curves in the EDS line-scanning profile revealed the uneven thickness of the dendritic nanostructure (Fig. 1(l)). EDS spectra showed that Bi and Se had an atomic ratio close to 2:3 in all three nanostructures (Fig. S1 in the Electronic Supplementary Material (ESM)).

To determine the crystalline structure of the three Bi_2Se_3 nanostructures, the XRD data provided in Fig. 3 indicated a rhombohedral crystalline structure for all samples (JCPDS No. 89-2008; a = 4.139 Å, c = 28.636 Å). However, for the spiral-type and smooth nanoplates, the diffraction peaks in (006) and (0, 0, 15) were both much stronger than the standard ones, which can be attributed to the enhancement in the diffraction in the vertical direction (z-axis). A high-quality single crystal for spiral-type and smooth nanoplates was revealed by selected area electron diffraction (SAED) patterns (insets in Figs. S2(a) and S2(c) in the ESM). In Figs. S2(b) and S2(d) (see ESM), HRTEM images of spiral-type and smooth nanoplates show lattice fringes with a lattice spacing of 0.21 nm, corresponding to the $(11\bar{2}0)$ planes. The polycrystalline characteristic of

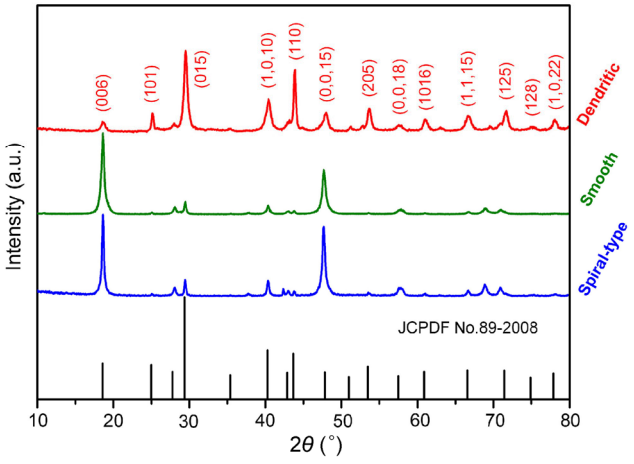

Figure 3 XRD patterns of spiral-type Bi_2Se_3 nanoplates, smooth Bi_2Se_3 nanoplates, and dendritic Bi_2Se_3 nanostructures. The dark columns at the bottom refer to standard JCPDS data for Bi_2Se_3.

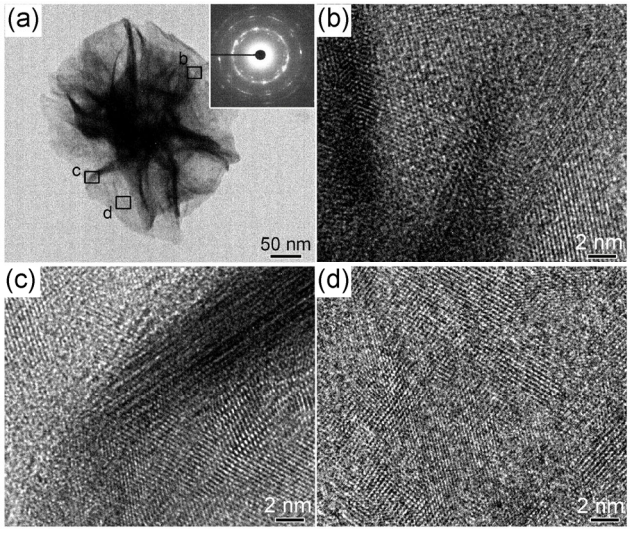

Figure 4 (a) TEM image of an individual dendritic Bi_2Se_3 nanostructure. The corresponding SAED pattern is shown in the inset. (b)–(d) HRTEM images of the three different regions marked in (a).

the dendritic nanostructures was confirmed by the SAED pattern in the inset of Fig. 4(a). HRTEM images of the regions indicated by boxes in Fig. 4(a) are shown in Figs. 4(b)–4(d), indicating different lattice orientations in these regions.

3.2 Shape evolution of three different Bi_2Se_3 nanostructures

To determine the growth process of the three different Bi_2Se_3 nanostructures, a series of TEM images were taken of samples obtained at different time points, as shown in Fig. 5. The formation process of spiral-type Bi_2Se_3 nanoplates is presented in Figs. 5(a)–5(d). After the rapid injection of both precursors into the reaction medium at 175 ˚C, the color of the solution gradually turned from faint yellow to light red. A Se sphere was observed in the initial stage (t = 6 min, Fig. 5(a)), and Bi_2Se_3 emerged later (t = 10 min, Fig. 5(b)). An incipient nanoplate appeared with a slip plane on the surface as the reaction continued (t = 20 min, Fig. 5(c)). Subsequently, growth along the step edge was observed (t = 40 min, Fig. 5(d)). With prolonged reaction, the product evolved into a well-defined spiral-type nanoplate (t = 2.5 h, Fig. 1(b)). A HAADF-STEM image of an individual nanostructure in Fig. 5(b) is presented in Fig. S3(a) (see ESM). As shown in Fig. S3(b) in the ESM, Bi_2Se_3 extending from the Se sphere had well-organized lattice fringes with a lattice spacing of 0.36 nm, which corresponded to the $(10\bar{1}1)$ planes. The single-crystal nature of exposed Bi_2Se_3 was revealed by the fast Fourier transform (FFT) pattern (inset of Fig. S3(b) in the ESM). The EDS elemental mapping images (Figs. S3(c)–S3(e) in the ESM) show that the content of Se was much higher than that of Bi. The HAADF image taken from the broken nanostructure caused by the irradiation of the high-energy electron beam indicated that the amorphous Se vanished, basically leaving only Bi_2Se_3 (Fig. S3(f) in the ESM). A random and overlapped deposition of single-crystal Bi_2Se_3 particles is observed in Fig. S3(g) in the ESM.

Since the addition of HCl can effectively lower the reducing capacity of AA [33], SeO_3^{2-} was initially reduced to a zero-valence Se sphere, which was confirmed by the change in the solution color from faint yellow to light red. The Se sphere grew larger as the reaction proceeded; meanwhile, some Se species were reduced further to form Bi_2Se_3. In the subsequent growth process, defects and stacking faults inevitably appeared because of the "imperfect" deposition of Bi_2Se_3 crystallites [34, 35], leading to the formation of a slip plane on the surface. Given that there is always a step edge to which atoms can be added on this occasion, the energy barrier to create new crystal steps can be overcome [36, 37]. Thus, the Bi_2Se_3 particles were continuously deposited along the step edge and

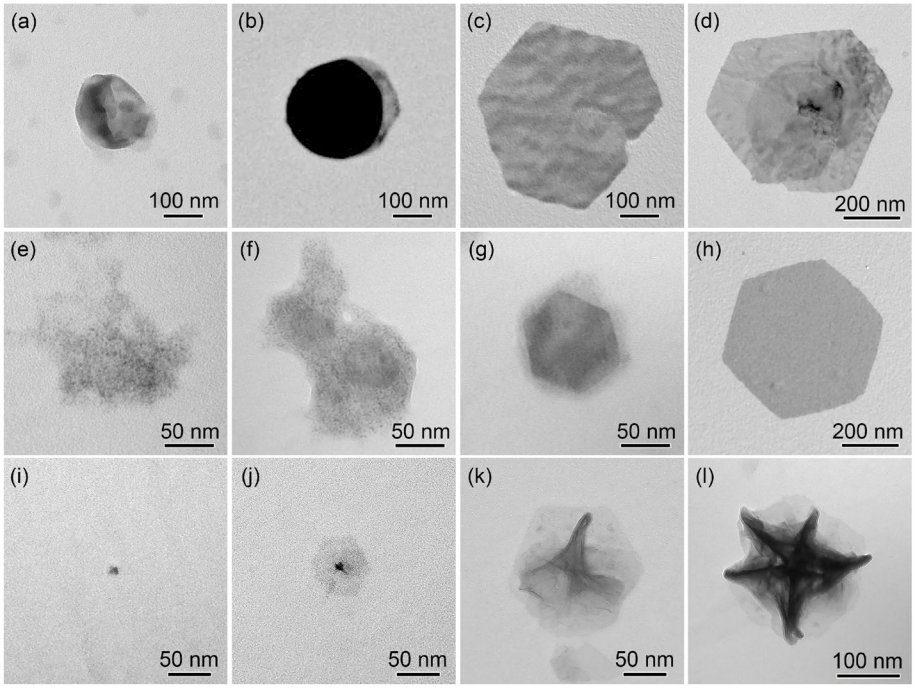

Figure 5 (a)–(d) TEM images of spiral-type Bi_2Se_3 nanoplates obtained at different time points: (a) 6 min, (b) 10 min, (c) 20 min, and (d) 40 min. (e)–(h) TEM images of smooth Bi_2Se_3 nanoplates obtained at different time points: (e) 70 s, (f) 100 s, (g) 140 s, and (h) 4 min. (i)–(l) TEM images of dendritic Bi_2Se_3 nanostructures obtained at different time points: (i) 10 s, (j) 30 s, (k) 1.5 min, and (l) 3 min.

lateral side, resulting in the formation of the final spiral-type Bi_2Se_3 nanoplates.

The formation process of smooth nanoplates is schematically illustrated in Figs. 5(e)–5(h). The color of the solution turned from faint yellow to light red immediately after the rapid injection of both precursors, indicating a faster reduction rate than that of spiral-type nanoplates. At the initial stage (t = 70 s, Fig. 5(e)), Bi_2Se_3 particles appeared in great abundance with an amorphous structure, as revealed by HRTEM and FFT analysis (Fig. S4 in the ESM). When the reaction proceeded to t = 100 s, these particles aggregated, forming a budding nanoplate (Fig. 5(f)). Afterwards, a larger nanoplate was observed with agglomerates around it (t = 140 s, Fig. 5(g)). The sample further developed into a mature Bi_2Se_3 nanoplate as the reaction continued (t = 4 min, Fig. 5(h) and t = 15 min, Fig. 1(f)). Different shapes (hexagonal and truncated triangular) coexist in Fig. 1(e), possibly owing to the formation of non-uniform budding nanoplates in the initial stage [38].

Figures 5(i)–5(l) display the growth process of dendritic Bi_2Se_3 nanostructures. After the rapid injection of both precursors, the color of the solution immediately changed from faint yellow to dark grey, indicating the fastest reaction rate among all the three synthetic processes. At the initial stage, small cores formed within t = 10 s (Fig. 5(i)), followed by random attachment of some irregular flakes (t = 30 s, Fig. 5(j)). The FFT pattern taken from the region (marked by a white box in Fig. S5(a) in the ESM) shows evidence of the polycrystalline characteristic of the core (inset in Fig. S5(b) in the ESM). Homogeneous distributions of Bi and Se were revealed by STEM-EDS mapping (Figs. S5(c)–S5(f) in the ESM). Subsequently, the sample grew larger (t = 1.5 min, Fig. 5(k)) with more branches protruding from the core (t = 3 min, Fig. 5(l)). Further development finally resulted in the formation of a typical dendritic Bi_2Se_3 nanostructure (t = 10 min, Fig. 1(j)).

3.3 Formation mechanism of Bi_2Se_3 nanostructures with different morphologies

It is indubitable that the supersaturation of the reaction system has a pivotal impact on crystal growth [39]. According to the classical crystal growth theory [40],

the supersaturation (σ) of a reaction system represents the driving force for crystal growth: $\sigma = \ln(c/c_0)$, where c is the Bi_2Se_3 concentration and c_0 is the equilibrium concentration. The growth rate (R) in different modes of crystal growth as a function of σ is presented in Fig. 6, where R continuously increases as the value of σ rises. In this work, σ was highly sensitive to the amount of HCl. Specifically, a greater amount of HCl weakened the reducing capacity of AA, leading to a lower σ. At low supersaturation, the energy barrier to nucleate new step edges was too high to be overcome; thus, the dislocation-driven growth dominated the crystal process, giving rise to the formation of spiral-type nanoplates. Since greater supersaturation can help nucleate new edge steps, layer-by-layer (LBL) growth started to dominate the process at intermediate supersaturation. Finally, fast nucleation and growth at high supersaturation promoted the generation of a number of "active centers" in the system. The nucleus could not grow along certain crystallographic directions [41], leading to dendritic growth in this situation.

To verify the regulatory role of supersaturation in the growth of different Bi_2Se_3 nanostructures, we varied the amount of AA with the other conditions unchanged. When a larger amount of AA was involved, the reduction was accelerated, resulting in a higher supersaturation of the system. Therefore, the modes of dislocation-driven growth, LBL growth, and dendritic growth are expected to progressively dominate the crystal growth when increasing the amount of AA. Figure S6 (see ESM) shows Bi_2Se_3 nanostructures

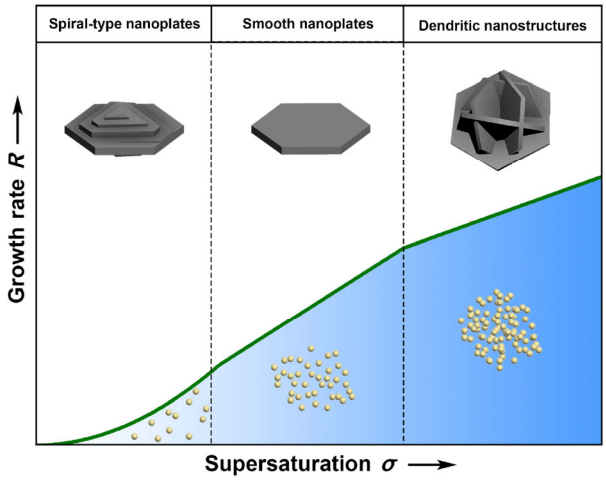

Figure 6 Schematic illustration of the growth rate in different modes of crystal growth as a function of the supersaturation.

prepared using different amounts of AA based on 20 μL of HCl. As expected, when a small amount of AA (43.5 mg) was used, spiral-type nanoplates constituted the majority of the resultant products (Fig. S6(a) in the ESM). A mixture containing spiral-type and smooth nanoplates was obtained when the amount of AA was increased to 64.8 mg (Fig. S6(b) in the ESM). When a larger amount of AA was added (174 mg), smooth nanoplates of high purity were produced (Figs. S6(c)–S6(e) in the ESM). When the amount of AA was further increased to 1,392 mg, dendritic nanostructures became an integral part of the final products (Fig. S6(f) in the ESM). In addition to the morphological modulation, this method can also achieve size control within a certain range. As shown in Figs. S6(c)–S6(e) in the ESM, when more AA was added, the size of smooth nanoplates became smaller. It is known that the size largely depends on the balance between the nucleation rate and the growth rate [42]. When more AA was introduced, a faster reduction rate was achieved, leading to the formation of more nuclei in the initial stage. In the subsequent growth stage, since the total amount of precursors was constant, less Bi_2Se_3 was deposited on each nucleus, resulting in the smaller size of the final nanoplates.

4 Conclusions

In summary, we demonstrated a polyol method for the shape-controlled synthesis of Bi_2Se_3 nanostructures through fine control of the supersaturation level. Specifically, by increasing the pH value or the amount of AA in the system, three different Bi_2Se_3 nanostructures including spiral-type nanoplates, smooth nanoplates, and dendritic nanostructures were obtained. A mechanism study indicated that the modes of dislocation-driven growth, LBL growth, and dendritic growth progressively dominated the crystal growth as the supersaturation increased. The inspiring results strengthen our confidence to fabricate Bi_2Se_3 and other nanostructures with rationally tunable morphologies.

Acknowledgements

This work was supported by Collaborative Innovation Center of Suzhou Nano Science and Technology,

MOST of China (No. 2014CB932700), 2015SRG-HSC049, National Natural Science Foundation of China (Nos. 21203173, 21573206, 11574281, 51371164, 51132007, and J1030412), Strategic Priority Research Program B of the CAS (No. XDB01020000), and Fundamental Research Funds for the Central Universities (Nos. WK2340000050, WK2060190025, and WK3510000002).

Electronic Supplementary Material: Supplementary material (EDS spectra of the three different Bi_2Se_3 nanostructures; TEM images, HRTEM images, and the corresponding SAED patterns of spiral-type and smooth Bi_2Se_3 nanoplates; HAADF-STEM image, HRTEM image, FFT pattern, STEM-EDS mapping, and HAADF image of the nanostructure obtained from the stage corresponding to Fig. 5(b); HRTEM image and fourier transform of the nanostructure obtained from the stage corresponding to Fig. 5(e); TEM image, HRTEM image, FFT pattern, and STEM-EDS mapping of the nanostructure obtained from the stage corresponding to Fig. 5(j); as well as TEM images of Bi_2Se_3 nanostructures obtained by using different amounts of AA on the basis of 20 μL of HCl) is available in the online version of this article at http://dx.doi.org/10.1007/s12274-015-0861-4.

References

[1] Moore, J. E. The birth of topological insulators. *Nature* **2010**, *464*, 194−198.

[2] Hasan, M. Z.; Kane, C. L. Topological insulators. *Rev. Mod. Phys.* **2010**, *82*, 3045−3067.

[3] Taskin, A. A.; Sasaki, S.; Segawa, K.; Ando, Y. Achieving surface quantum oscillations in topological insulator thin films of Bi_2Se_3. *Adv. Mater.* **2012**, *24*, 5581−5585.

[4] Peng, H. L.; Dang, W. H.; Cao, J.; Chen, Y. L.; Wu, D.; Zheng, W. S.; Li, H.; Shen, Z. X.; Liu, Z. F. Topological insulator nanostructures for near-infrared transparent flexible electrodes. *Nat. Chem.* **2012**, *4*, 281−286.

[5] Qi, X. L.; Zhang, S. C. Topological insulators and superconductors. *Rev. Mod. Phys.* **2011**, *83*, 1057−1110.

[6] Kong, D. S.; Cui, Y. Opportunities in chemistry and materials science for topological insulators and their nanostructures. *Nat. Chem.* **2011**, *3*, 845−849.

[7] Müchler, L.; Casper, F.; Yan, B. H.; Chadov, S.; Felser, C. Topological insulators and thermoelectric materials. *Phys. Status Solidi RRL* **2013**, *7*, 91−100.

[8] Wyckoff, R. W. G. *Crystal Structures;* Krieger: Malabar, FL, 1986.

[9] Zhang, H. J.; Liu, C. X.; Qi, X. L.; Dai, X.; Fang, Z.; Zhang, S. C. Topological insulators in Bi_2Se_3, Bi_2Te_3 and Sb_2Te_3 with a single Dirac cone on the surface. *Nat. Phys.* **2009**, *5*, 438−442.

[10] Xia, Y.; Qian, D.; Hsieh, D.; Wray, L.; Pal, A.; Lin, H.; Bansil, A.; Grauer, D.; Hor, Y. S.; Cava, R. J. et al. Observation of a large-gap topological-insulator class with a single Dirac cone on the surface. *Nat. Phys.* **2009**, *5*, 398−402.

[11] Zareapour, P.; Hayat, A.; Zhao, S. Y. F.; Kreshchuk, M.; Jain, A.; Kwok, D. C.; Lee, N.; Cheong, S. W.; Xu, Z. J.; Yang, A. et al. Proximity-induced high-temperature superconductivity in the topological insulators Bi_2Se_3 and Bi_2Te_3. *Nat. Commun.* **2012**, *3*, 1056.

[12] Sun, L. P.; Lin, Z. Q.; Peng, J.; Weng, J.; Huang, Y. Z.; Luo, Z. Q. Preparation of few-layer bismuth selenide by liquid-phase-exfoliation and its optical absorption properties. *Sci. Rep.* **2014**, *4*, 4794.

[13] Zhang, X.; Wang, J.; Zhang, S. C. Topological insulators for high-performance terahertz to infrared applications. *Phys. Rev. B* **2011**, *82*, 245107.

[14] Zhao, C. J.; Zou, Y. H.; Chen, Y.; Wang, Z. T.; Lu, S. B.; Zhang, H.; Wen, S. C.; Tang, D. Y. Wavelength-tunable picosecond soliton fiber laser with topological insulator: Bi_2Se_3 as a mode locker. *Opt. Express* **2012**, *20*, 27888−27895.

[15] Li, J.; Jiang, F.; Yang, B.; Song, X. R.; Liu, Y.; Yang, H. H.; Cao, D. R.; Shi, W. R.; Chen, G. N. Topological insulator bismuth selenide as a theranostic platform for simultaneous cancer imaging and therapy. *Sci. Rep.* **2013**, *3*, 1998.

[16] Sun, Y. F.; Cheng, H.; Gao, S.; Liu, Q. H.; Sun, Z. H.; Xiao, C.; Wu, C. Z.; Wei, S. Q.; Xie, Y. Atomically thick bismuth selenide freestanding single layers achieving enhanced thermoelectric energy harvesting. *J. Am. Chem. Soc.* **2012**, *134*, 20294−20297.

[17] Soni, A.; Zhao, Y. Y.; Yu, L. G.; Aik, M. K. K.; Dresselhaus, M. S.; Xiong, Q. H. Enhanced thermoelectric properties of solution grown $Bi_2Te_{3-x}Se_x$ nanoplatelet composites. *Nano Lett.* **2012**, *12*, 1203−1209.

[18] Min, Y.; Roh, J. W.; Yang, H.; Park, M.; Kim, S. I.; Hwang, S.; Lee, S. M.; Lee, K. H.; Jeong, U. Surfactant-free scalable synthesis of Bi_2Te_3 and Bi_2Se_3 nanoflakes and enhanced thermoelectric properties of their nanocomposites. *Adv. Mater.* **2013**, *25*, 1425−1429.

[19] Yu, J. K.; Mitrovic, S.; Than, D.; Varghese, J.; Heath, J. R. Reduction of thermal conductivity in phononic nanomesh structures. *Nat. Nanotechnol.* **2010**, *5*, 718−721.

[20] Son, J. S.; Park, K.; Han, M. K.; Kang, C.; Park, S. G.; Kim,

J. H.; Kim, W.; Kim, S. J.; Hyeon, T. Large-scale synthesis and characterization of the size-dependent thermoelectric properties of uniformly sized bismuth nanocrystals. *Angew. Chem., Int. Ed.* **2011**, *123*, 1399−1402.

[21] Zuev, Y. M.; Lee, J. S.; Galloy, C.; Park, H.; Kim, P. Diameter dependence of the transport properties of antimony telluride nanowires. *Nano Lett.* **2010**, *10*, 3037−3040.

[22] Dirmyer, M. R.; Martin, J.; Nolas, G. S.; Sen, A.; Badding, J. V. Thermal and electrical conductivity of size-tuned bismuth telluride nanoparticles. *Small* **2009**, *5*, 933−937.

[23] Linder, J.; Yokoyama, T.; Sudbø, A. Anomalous finite size effects on surface states in the topological insulator Bi_2Se_3. *Phys. Rev. B* **2009**, *80*, 205401.

[24] Zhang, Y.; He, K.; Chang, C. Z.; Song, C. L.; Wang, L. L.; Chen, X.; Jia, J. F.; Fang, Z.; Dai, X.; Shan, W. Y. et al. Crossover of the three-dimensional topological insulator Bi_2Se_3 to the two-dimensional limit. *Nat. Phys.* **2010**, *6*, 584−588.

[25] Fan, H.; Zhang, S. X.; Ju, P.; Su, H. C.; Ai, S. Y. Flower-like Bi_2Se_3 nanostructures: Synthesis and their application for the direct electrochemistry of hemoglobin and H_2O_2 detection. *Electrochim. Acta* **2012**, *64*, 171−176.

[26] Yao, J.; Koski, K. J.; Luo, W. D.; Cha, J. J.; Hu, L. B.; Kong, D. S.; Narasimhan, V. K.; Huo, K. F.; Cui, Y. Optical transmission enhacement through chemically tuned two-dimensional bismuth chalcogenide nanoplates. *Nat. Commun.* **2014**, *5*, 5670.

[27] Xu, S.; Zhao, W. B.; Hong, J. M.; Zhu, J. J.; Chen, H. Y. Photochemical synthesis of Bi_2Se_3 nanosphere and nanorods. *Mater. Lett*. **2005**, *59*, 319−321.

[28] Zhuang, A. W.; Zhao, Y. Z.; Liu, X. L.; Xu, M. R.; Wang, Y. C.; Jeong, U.; Wang, X. P.; Zeng, J. Controlling the lateral and vertical dimensions of Bi_2Se_3 nanoplates via seeded growth. *Nano Res.* **2015**, *8*, 246−256.

[29] Min, Y.; Moon, G. D.; Kim, B. S.; Lim, B.; Kim, J. S.; Kang, C. Y.; Jeong, U. Quick, controlled synthesis of ultrathin Bi_2Se_3 nanodiscs and nanosheets. *J. Am. Chem. Soc.* **2012**, *134*, 2872−2875.

[30] Zhang, J.; Peng, Z. P.; Soni, A.; Zhao, Y. Y.; Xiong, Y.; Peng, B.; Wang, J. B.; Dresselhaus, M. S.; Xiong, Q. H. Raman spectroscopy of few-quintuple layer topological insulator Bi_2Se_3 nanoplatelets. *Nano Lett.* **2011**, *11*, 2407−2414.

[31] Sun, Z. L.; Liufu, S.; Chen, X. H.; Chen, L. D. Controllable synthesis and electrochemical hydrogen storage properties of Bi_2Se_3 architectural structures. *Chem. Commun.* **2010**, *46*, 3101−3103.

[32] Zhuang, A. W.; Li, J. J.; Wang, Y. C.; Wen, X.; Lin, Y.; Xiang, B.; Wang, X. P.; Zeng, J. Screw-dislocation-driven bidirectional spiral growth of Bi_2Se_3 nanoplates. *Angew. Chem., Int. Ed.* **2014**, *126*, 6543−6547.

[33] Zhou, J. H.; Zeng, J.; Grant, J.; Wu, H. K.; Xia, Y. N. On-chip screening of experimental conditions for the synthesis of noble-metal nanostructures with different morphologies. *Small* **2011**, *7*, 3308−3316.

[34] Jin, S.; Bierman, M. J.; Morin, S. A. A new twist on nanowire formation: Screw-dislocation-driven growth of nanowires and nanotubes. *J. Phys. Chem. Lett*. **2010**, *1*, 1472−1480.

[35] Penn, R. L.; Banfield, J. F. Imperfect oriented attachment: Dislocation generation in defect-free nanocrystals. *Science* **1998**, *281*, 969−971.

[36] Hirth, J. P.; Lothe, J. *Theory of Dislocations;* MaGraw-Hill: New York, 1968.

[37] Burton, W. K.; Cabrera, N.; Frank, F. C. Role of dislocations in crystal growth. *Nature* **1949**, *163*, 398−399.

[38] Xia, Y. N.; Xia, X. H.; Peng, H. C. Shape-controlled synthesis of colloidal metal nanocrystals: Thermodynamic versus kinetic products. *J. Am. Chem. Soc.* **2015**, *137*, 7947−7966.

[39] Meng, F.; Morin, S. A.; Forticaux, A.; Jin, S. Screw dislocation driven growth of nanomaterials. *Acc. Chem. Res.* **2013**, *46*, 1616−1626.

[40] Markov, I. V. *Crystal Growth for Beginners: Fundamentals of Nucleation, Crystal Growth, and Epitaxy;* World Scientific Publishing Co. Pte. Ltd.: Singapore, 1995.

[41] Zhuo, R. F.; Feng, H. T.; Chen, J. T.; Yan, D.; Feng, J. J.; Li, H. J.; Geng, B. S.; Cheng, S.; Xu, X. Y.; Yan, P. X. Multistep synthesis, growth mechanism, optical, and microwave absorption properties of ZnO dendritic nanostructures. *J. Phys. Chem. C* **2008**, *112*, 11767−11775.

[42] Shevchenko, E. V.; Talapin, D. V.; Schnablegger, H.; Kornowski, A.; Festin, Ö.; Svedlindh, P.; Haase, M.; Weller, H. Study of nucleation and growth in the organometallic synthesis of magnetic alloy nanocrystals: The role of nucleation rate in size control of $CoPt_3$ nanocrystals. *J. Am. Chem. Soc.* **2003**, *125*, 9090−9101.